Modeling of a multi-section transformer for a modular high-voltage DC–DC converter

Paweł Milewski
Zakład Automatyki i Urządzeń Pomiarowych AREX Sp. z o.o.
Gdańsk University of Technology, Implementation Doctoral School
Gdynia, Poland
https://orcid.org/0009-0000-4459-8428

***Abstract*— The paper presents the architecture of a modular high-voltage DC–DC converter employing SiC-based switching devices. The developed system consists of four 2 kW modules (320 V DC / 0–50 kV DC). A key component of the converter is a multi-section high-voltage transformer with a proposed 3×(1P2S) configuration, incorporating a common-mode (CM) filter on the primary side. Based on a simulation model, an analytical model of the multi-section transformer, including the impact of the CM filter, was developed. A frequency-domain analysis was performed to identify the influence of the transformer equivalent circuit parameters on the operating conditions of the converter resonant circuit. The transformer design analysis also considered, among other aspects, the need to reduce the secondary-side winding capacitance. The validity of the proposed model was verified through comparison of analytical results with experimental measurements. The conducted analysis demonstrated a significant influence of the multi-section transformer winding structure on the functional characteristics of the resonant converter, particularly on the voltage gain characteristics.**

Keywords—HV SiC converter, parasitic capacitance mitigation, multi-section transformer, transformer modelling

I. INTRODUCTION

The current development trend in high-voltage power converters is strongly associated with the widespread adoption of SiC transistors and diodes. The material properties of 4H-SiC semiconductor devices provide significant operational advantages over conventional silicon-based components. High-voltage components manufactured using SiC technology are characterized by lower switching losses, which is directly related to their superior dynamic performance [1], [2]. The high dielectric strength of SiC semiconductors enables the implementation of high-voltage structures while maintaining a relatively small active area. At the same time, advances in SiC transistor and power module manufacturing technologies have led to the emergence of commercially available components in the 3.3 kV, 6.5 kV, and 10 kV voltage classes [3], [4].

High-voltage power electronic converters are widely used across numerous industrial sectors. Examples of their applications include:

- surface corona treatment for improving paint and coating adhesion in the plastics and paper industries [5], [6],
- ion and electron beam lithography for semiconductor structure fabrication in the electronics industry [7],
- plasma nitriding and plasma-assisted heat treatment processes in the metallurgical industry [8],
- plasma-assisted chemical synthesis, ozone generation, and capillary electrophoresis in the chemical industry [9],
- X-ray power supplies used in medical equipment and industrial diagnostics [10],
- high-voltage test generators used in measurement systems for testing transformers, cables, and other high-voltage equipment [11],
- high-voltage direct current (HVDC) transmission systems in the power industry [12], [13],
- systems used as components of high-power microwave (HPM) weapons in the defense industry [14].

The intended application of a power supply system involved in the electrical energy conversion process is of significant importance in the context of converter topology selection, cooling method, insulation requirements, and environmental as well as operating conditions. The electrical insulation strength of HV transformers is particularly important due to the stresses associated with high $\mathrm{d}u/\mathrm{d}t$ values resulting from switching transitions of power semiconductor devices. This leads to accelerated degradation of insulation parameters related, among others, to dielectric losses and the occurrence of partial discharges [15]. This issue is particularly significant in hard-switching topologies, where steep voltage transitions occur directly across transformer windings and correspond to the voltage transitions of converter semiconductor switches. In step-up transformers, the amplitude of these stresses is additionally increased due to the transformer turns ratio, while maintaining a very short voltage rise time. This phenomenon becomes even more critical when wide-bandgap semiconductor devices, such as SiC-based switches characterized by superior dynamic performance, are employed. In dry-type transformers used in SST systems and encapsulated in epoxy resin, dielectric losses may account for up to 17% of the total transformer power losses. In extreme cases, this may lead to thermal runaway and consequently transformer failure. Significant reduction of insulation stresses can be achieved through the application of multilevel topologies and soft-switching converters, e.g., resonant converters [16].

The characteristics of the resonant DC–DC converter analyzed in this paper require the application of a high-voltage transformer. The rated input voltage of a single converter module is 320 V DC (MV side), with an adjustable output voltage in the range of 0–12.5 kV DC. The rated power of a single module is 2 kW, with a maximum high-voltage output current of 200 mA. Series connection of four modules on the secondary side enables output voltage regulation within the range of 0–50 kV DC (HV side). The transformer test voltage is specified as 100 kV DC for 1 min. Requirements related to transformer insulation strength, symmetrical electrical parameters of individual transformer sections, and reduction of secondary-side parasitic capacitances significantly affect the magnetic

979-8-3195-0938-3/26/$31.00 ©2026 IEEE

structure design process. Therefore, the development of a nonstandard transformer spatial arrangement and a dedicated insulation system was required

II. Modular High-Voltage DC–DC Converter

Due to the necessity of reducing du/dt stresses imposed on the transformer insulation and the widespread availability of 3.3 kV SiC diodes, a resonant topology with a multi-section transformer was selected. The design process of the HV DC–DC converter was initiated with the transformer design, which directly determined both the modular and submodule-level converter structure. The development of the insulation system for the high-voltage section constituted one of the major challenges in the converter design process. Based on finite-element field analysis performed in Ansys and frequency-domain measurements of two transformer models, the necessity of employing transformers with symmetrical capacitance distribution between individual sections was identified. This was found to be particularly important due to discrepancies in the operating points of the resonant circuit between individual sections. Fig. 1 presents the first transformer prototype and the final transformer in the proposed 3×(1P2S) configuration integrated into an insulated PA12 polyamide enclosure. The primary reason for rejecting the first transformer prototype was the nonuniform interwinding capacitance observed between individual submodules, particularly the capacitance between the primary- and secondary-side windings.

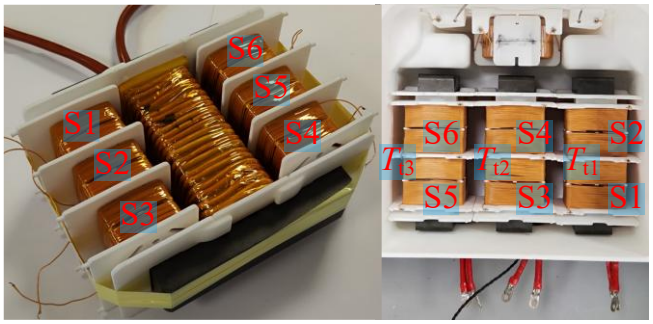


Fig. 1. The first transformer prototype (left) and the final transformer in a 3×(1P2S) configuration integrated into a PA12 polyamide structure with marked sections S1..6 (right)

The proposed converter structure is based on a modular approach. A simplified schematic diagram of the considered modular converter is shown in Fig. 2. The system consists of four modules (M1..4) connected in parallel on the primary side and in series on the secondary side. Each module consists of a full-bridge transistor inverter on the primary side and six submodules (SM1..6) on the secondary side. The maximum output voltage of each submodule is approximately 2.1 kV. Due to the requirement for passive cooling, wide-bandgap SiC semiconductor devices were selected in order to reduce power losses and consequently improve overall converter efficiency. The applied rectifier diodes are merged pn-Schottky (MPS) diodes [17].

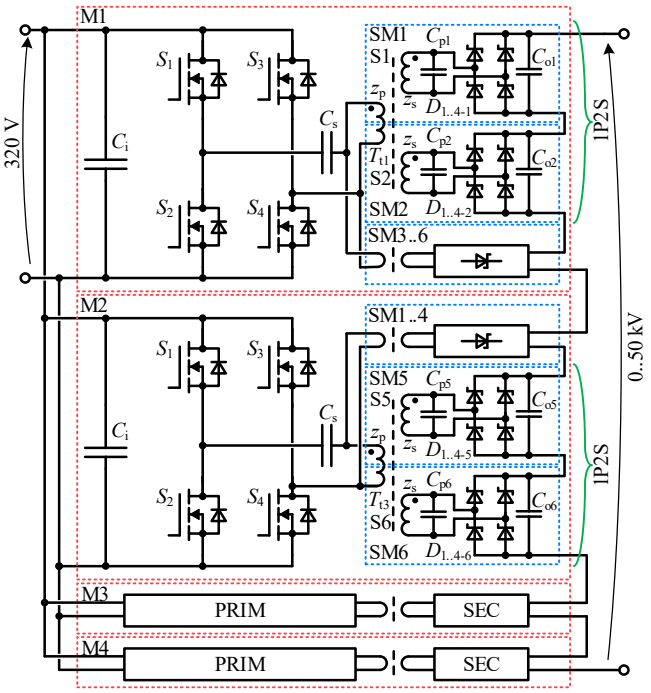


Fig. 2. Modular resonant converter structure with a multi-section transformer

Fig. 2 illustrates: C_i – converter input capacitor, $S_{1..4}$ – transistors in the full-bridge configuration, C_s – main resonant circuit capacitor, $T_{t1..3}$ – sectional transformers assigned to subsequent pairs of submodules SM1..6, $C_{p1..6}$ – capacitors representing the secondary-side parasitic capacitances of individual transformer sections, $D_{1..4\text{-}1..6}$ – rectifier bridge diodes, $C_{o1..6}$ – output capacitors of submodules SM1..6, z_p – number of primary-side turns, z_s – number of secondary-side turns of an individual section, S1..6 – secondary-side sections of transformers $T_{t1..3}$ and 1P2S – a structure corresponding to two submodules as well as transformers $T_{t1..3}$.

During experimental investigations of the converter, challenges related to disturbances affecting the controller operation were observed, particularly in the fiber-optic HV voltage measurement interface. This issue occurred mainly during step load transients. Therefore, additional methods for reducing conducted and radiated emissions were required. One of the key elements of the system was a six-winding common-mode (CM) filter implemented between the main resonant circuit capacitor C_s and the primary windings of transformers $T_{t1..3}$ (Fig. 3). According to the design assumptions, the filter performs three primary functions:

- increasing the common-mode impedance within a specified frequency range in order to reduce the impact of the HV section on the microprocessor-based control system located on the MV side,
- equalizing (balancing) currents in the three transformer submodules ($T_{t1..3}$) connected to a common transistor bridge,
- increasing the transformer leakage inductance, enabling the main resonant frequency to be shifted toward lower frequencies.



Fig. 3. Prototype of the toroidal six-winding CM filter (CM_2)

The impact of the six-winding CM filter on the resonant circuit characteristics is significant. The dominant influence on the voltage gain characteristic of the resonant converter is associated with the differential-mode (DM) component of the CM filter corresponding to the leakage inductance [18]. Fig. 4 presents the resonant circuit extended with the CM filter model. This circuit constitutes the basis for the further analysis presented in this paper.

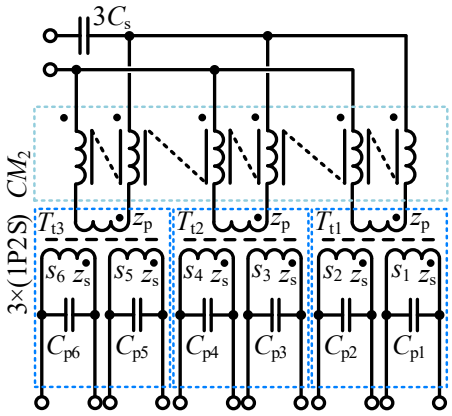


Fig. 4. Final resonant circuit of the modular converter extended with the CM filter on the transformer primary side

III. Frequency-Domain Analysis

The development of the equivalent model of the resonant circuit, consisting of the resonant tank capacitor (RTK), a six-winding common-mode choke (CMC), and the transformer (TRR), was initiated by defining an expected simplified equivalent circuit, shown in Fig. 5. The model was subsequently extended to include parasitic elements. In particular, the resonant capacitor was represented by a series RLC network (R_s, L_s, C_s). The CMC model was introduced in a simplified two-winding form, primarily representing the differential-mode (DM) components (R_{dCM}, L_{dCM}), while also accounting for the parallel capacitance C_{pCM} [19]. The transformer was also modeled in a simplified form as a single 1P2S structure consisting of one primary winding and two secondary-side windings (S1 and S2). The model, including the magnetizing inductance (L_m) and leakage inductances ($L_{\sigma 0}$, $L_{\sigma 1}$, $L_{\sigma 2}$), was further extended to incorporate interwinding capacitances (C_{01}, C_{02}) and intrawinding capacitances (C_{p0}, C_{p1}, C_{p2}). Resistances R_0, R_1 and R_2 represent the equivalent winding resistances, whereas R_f is associated with transformer core power losses. Parameters z_p and z_s denote the number of turns of the primary and secondary windings, respectively.

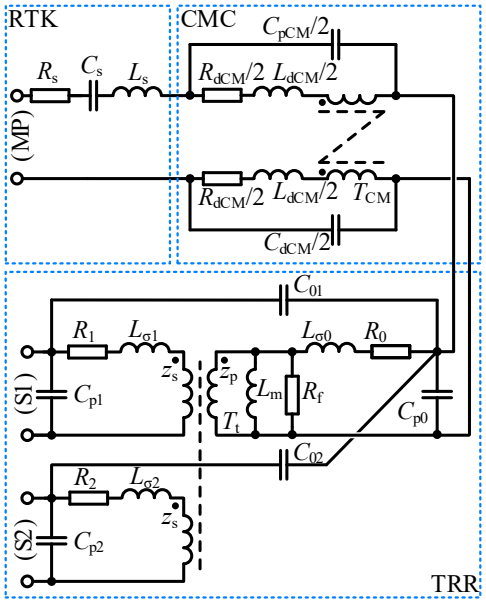


Fig. 5. Simplified equivalent circuit of the high-voltage converter resonant tank

In the next stage of the investigation, a frequency-domain analysis was conducted to align the frequency characteristics of the fabricated transformer with those obtained from the simulation model. The measurement results revealed that, for frequencies above 1 MHz, the frequency response is strongly affected by the secondary-side parasitic capacitances and the interwinding capacitances between the primary and secondary windings. The equivalent circuit that demonstrated the best agreement with the measured frequency characteristics is shown in Fig. 6.

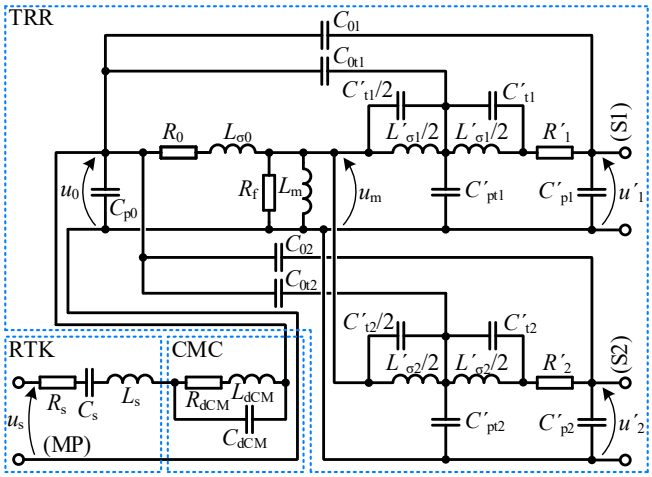


Fig. 6. Extended equivalent circuit of the resonant tank of the high-voltage converter for a single 1P2S transformer

Transformer parameter identification was performed based on the analysis of frequency characteristics determined for two operating conditions, namely short-circuit and open-circuit states, using measurements carried out with a vector network analyzer from both the primary- and secondary-side terminals. Additional investigations were conducted to assess the correctness of the identified equivalent circuit parameters, including measurements of the primary winding with the core installed but without the secondary winding. To simplify the transformer modeling

process, symmetry of the transformer secondary side was assumed, i.e., the parameters of secondary-side windings S1 and S2 were considered identical (C_{tn}, $L_{\sigma n}$, R_n, C_{ptn}, C_{pn}). The equivalent circuit parameters were referred between the secondary and primary sides using the relations given in (1) and (2). The parameters denoted by a prime symbol in Fig. 6 represent secondary-side values referred to the primary side.

$$R'_{\mathrm{x}} = R_{\mathrm{x}}\left(\frac{z_{\mathrm{p}}}{z_{\mathrm{s}}}\right)^2,\ L'_{\mathrm{x}} = L_{\mathrm{x}}\left(\frac{z_{\mathrm{p}}}{z_{\mathrm{s}}}\right)^2,\ C'_{\mathrm{x}} = C_{\mathrm{x}}\left(\frac{z_{\mathrm{s}}}{z_{\mathrm{p}}}\right)^2 \quad (1)$$

$$Z'_{\mathrm{x}} = Z_{\mathrm{x}}\left(\frac{z_{\mathrm{p}}}{z_{\mathrm{s}}}\right)^2,\ u'_{\mathrm{x}} = u_{\mathrm{x}}\frac{z_{\mathrm{p}}}{z_{\mathrm{s}}} \quad (2)$$

The key relations used for parameter identification under short-circuit conditions, from the primary and secondary sides, respectively, were given by (4) and (5). The analysis was further supplemented by (6), associated with the identification of the primary-side parameters with the secondary winding removed. These relations enabled an initial estimation of the leakage and magnetizing inductances based on inductance measurements (L_{pr} = 56 µH, L_{se} = 1761 µH, L_{pws} = 1165 µH) performed using the analyzer at a frequency of 10 kHz.

$$L_{\mathrm{pr}} \approx L_{\sigma 0} + \frac{L_{\mathrm{m}}L'_{\sigma n}}{2L_{\mathrm{m}} + L'_{\sigma n}} \quad (4)$$

$$L_{\mathrm{se}} \approx L_{\sigma n} + \frac{L'_{\sigma 0}L_{\sigma n}L'_{\mathrm{m}}}{L_{\sigma n}L'_{\mathrm{m}} + L'_{\sigma 0}L_{\sigma n} + L'_{\sigma 0}L'_{\mathrm{m}}} \quad (5)$$

$$L_{\mathrm{pws}} \approx L_{\sigma 0} + L_{\mathrm{m}} \quad (6)$$

Subsequently, iterative tuning of the equivalent circuit parameters was carried out using circuit simulations in order to achieve the best possible agreement with the characteristics of the experimental model. The values of the extended equivalent circuit parameters referred to the secondary side (S*n*) are listed in Table I.

TABLE I. SECONDARY-REFERRED EQUIVALENT TRANSFORMER CIRCUIT PARAMETERS

Symbol	***Value***
$C'_{\mathrm{p}0}$	0.3 pF
$L'_{\sigma 0}$	1.688 mH
R'_0	0.52 Ω
R'_{f}	1 MΩ
L'_{m}	46.695 mH
$C_{t1} = C_{t2} = C_{tn}$	8 pF
$L_{\sigma 1} = L_{\sigma 2} = L_{\sigma n}$	1.208 mH
$C_{pt1} = C_{pt2} = C_{ptn}$	0.5 pF
$R_1 = R_2 = R_n$	2.3 Ω
$C_{p1} = C_{p2} = C_{pn}$	14.5 pF
$C_{01} = C_{02} = C_{0n}$	0.5 pF
$C_{0t1} = C_{0t2} = C_{0tn}$	1 pF
$z_{\mathrm{s}} / z_{\mathrm{p}}$	116/18

Using the parameters listed in Table I, transformer impedance frequency characteristics were generated for different operating conditions, including open-circuit and short-circuit conditions (1P2S structure). Experimental measurements were performed on the transformer prior to silicone potting. Due to the low-voltage output signal of the measurement analyzer, the value of the resistance R_{f}, associated with transformer core losses, was assumed to be 1 MΩ. In the model adjusted to the target converter supply voltage (320 V DC), the value of R_{f} should be approximately 33 kΩ, corresponding to estimated hysteresis core losses of approximately 3.1 W for each 1P2S structure. These core losses correspond to a magnetic flux density amplitude of approximately 105 mT at an operating frequency of 75.8 kHz.

Fig. 7 presents the transformer impedance frequency characteristics under open-circuit conditions, determined from the secondary-side winding terminals (S1), i.e., with the primary winding and the winding of the second secondary-side submodule left open. Good agreement can be observed between the characteristics obtained from the physical transformer and the simulation model based on the extended equivalent circuit (Fig. 6). The most significant discrepancies occur above 1 MHz and are associated with the complex nature of the secondary-side parasitic capacitances. The resonance observed around 2.5 MHz is associated with the resonance formed by the secondary winding section and its intrawinding capacitance ($L_{\sigma 1}/2$, C_{tn}).

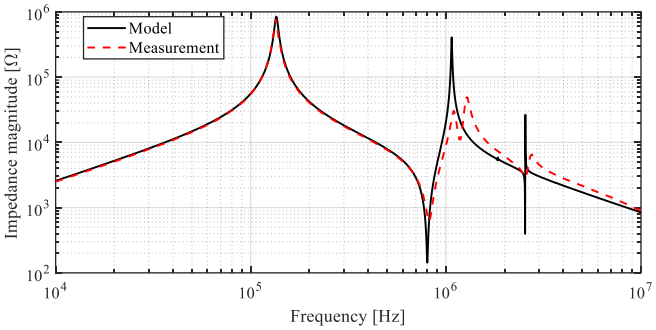


Fig. 7. Transformer impedance frequency characteristics under open-circuit conditions at the secondary-side winding for the simulation model and measurements performed on the fabricated transformer

The characteristics presented in Fig. 8 correspond to the transformer short-circuit condition on the primary side (MP) and at the terminals of secondary-side winding S2 (u_0 = 0 V, u_2 = 0 V), while the measurement was performed from the terminals of secondary-side winding S1. Despite the change in transformer operating conditions, the resonance around 2.5 MHz remains visible, which may confirm its association with the internal resonance of the secondary winding. To further verify the validity of the model, a comparison of the characteristics determined from the primary-side terminals was performed. After appropriately referring the equivalent circuit parameters from Table I according to (1), and subsequently introducing them into the simulation model, the characteristic shown in Fig. 9 was generated. This characteristic corresponds to open-circuit conditions, i.e., with S1 and S2 windings left open. Compared with the measurement results, the characteristic obtained from the simulation model exhibits stronger damping of the resonances below 1 MHz, manifested by smoother and more flattened resonance peaks. Above 1 MHz, the opposite tendency is observed.

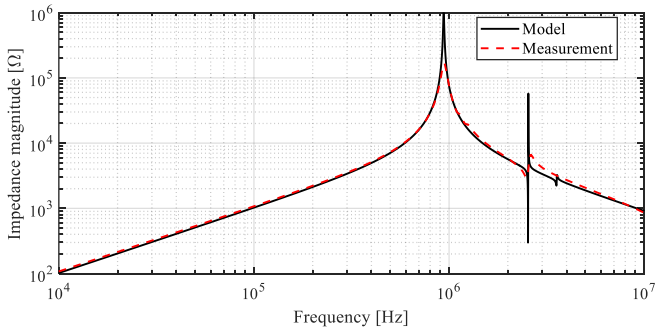


Fig. 8. Transformer impedance frequency characteristics under short-circuit conditions ($u_0 = 0$ V, $u_2 = 0$ V) at the secondary-side winding (S1) for the simulation model and measurements performed on the fabricated transformer

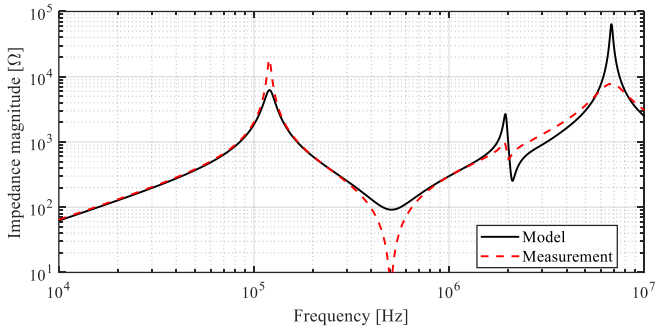


Fig. 9. Transformer impedance frequency characteristics under open-circuit conditions at the primary-side winding (MP) for the simulation model and measurements performed on the fabricated transformer

As mentioned earlier, in the final experimental model, the transformer chamber of the 3×(1P2S) structure (Fig. 1, right) was filled with a silicone compound in order to ensure an adequate transformer insulation system. The ELASTOSIL RT silicone potting material was selected due to its declared dielectric strength of 23 kV/mm and low dielectric loss factor (dissipation factor) tanδ. ELASTOSIL RT exhibits an almost frequency-independent tanδ characteristic, which is advantageous for high-voltage power electronics applications [19]. Since an increase in parasitic capacitances was expected after potting, comparative frequency-response measurements of the transformer before and after silicone potting were performed (Fig. 10). The measurements were carried out under open-circuit conditions, determined from the secondary-side winding terminals (S1). An increase in parasitic capacitances by approximately 1.64–1.73 times was observed, resulting in a shift of the frequency characteristics toward lower frequencies.

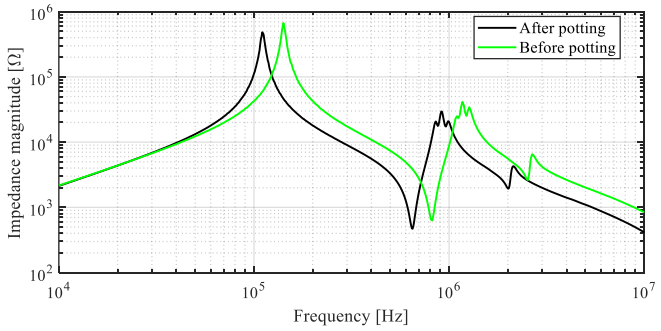


Fig. 10. Transformer impedance frequency characteristics under open-circuit conditions at the secondary-side winding (Sn) before and after silicone potting

IV. Analytical Model of the Transformer

The analytical model development for the transformer (1P2S structure) was initiated by introducing simplifying assumptions. Due to the assumed operating frequency range of the resonant converter, the analytical model was intended to accurately reproduce the system characteristics up to 1 MHz. Consequently, the parasitic capacitances C_{0n}, C_{0tn} and C_{tn} were neglected in the subsequent analysis. The development of the proposed analytical model in the s-domain began with the formulation of impedance expressions for the individual parts of the circuit. For this purpose, the input impedances Z_{p0} and Z_0 were defined according to (7), the magnetizing impedance Z_m according to (8), and the output impedances Z'_n and Z'_{pn} referred to the primary side according to (9).

$$Z_{p0}(s) = \frac{1}{sC_{p0}},\ Z_0(s) = R_0 + sL_{\sigma 0} \tag{7}$$

$$Z_m(s) = \frac{R_f sL_m}{R_f + sL_m} \tag{8}$$

$$Z'_n(s) = R'_n + sL'_{\sigma n},\ Z'_{pn}(s) = \frac{1}{sC'_{pn}} \tag{9}$$

The general analytical model is described by the set of relations given in (10)–(13).

$$\frac{u_0(s)}{Z_{p0}(s)} + \frac{u_0(s) - u_m(s)}{Z_0(s)} = 0 \tag{10}$$

$$\frac{u_m(s) - u_0(s)}{Z_0(s)} + \frac{u_m(s)}{Z_m(s)} + \frac{u_m(s) - u'_1(s)}{Z'_n(s)} + \frac{u_m(s) - u'_2(s)}{Z'_n(s)} = 0 \tag{11}$$

$$\frac{u'_1(s) - u_m(s)}{Z'_n(s)} + \frac{u'_1(s)}{Z'_{pn}(s)} = 0 \tag{12}$$

$$\frac{u'_2(s) - u_m(s)}{Z'_n(s)} + \frac{u'_2(s)}{Z'_{pn}(s)} = 0 \tag{13}$$

To compare the frequency characteristics obtained from experimental measurements, the simulation model, and the analytical model, the ratio u'_1/i'_1 corresponding to the secondary-side measurements was determined as an example for two operating conditions: open-circuit, described by (15), and short-circuit, described by (17). For clarity, two magnetizing impedances were defined: $Z_{m\text{-}oc}$ for the open-circuit condition (14) and $Z_{m\text{-}sc}$ for the short-circuit condition (16). For the short-circuit condition, with the measurement performed from the S2 terminals, $u_0 = 0$ V and $u'_2 = 0$ V were assumed.

Open-circuit condition, measurement from the S1:

$$Z_{m\text{-}oc}(s) = \left[\frac{1}{Z_m(s)} + \frac{1}{Z_0(s) + Z_{p0}(s)} + \frac{1}{Z'_n(s) + Z'_{pn}(s)}\right]^{-1} \tag{14}$$

$$Z'_{sec\text{-}oc}(s) = \frac{u'_1(s)}{i'_1(s)} = \left[\frac{1}{Z'_{pn}(s)} + \frac{1}{Z'_n(s) + Z_{m\text{-}oc}(s)}\right]^{-1} \tag{15}$$

Short-circuit condition, measurement from the S1:

$$Z_{\text{m-sc}}(s)=\left[\frac{1}{Z_{\text{f}}(s)}+\frac{1}{Z_0(s)}+\frac{1}{Z'_n(s)}\right]^{-1} \tag{16}$$

$$Z'_{\text{sec-sc}}(s)=\frac{u'_1(s)}{i'_1(s)}=\left[\frac{1}{Z'_{\text{pn}}(s)}+\frac{1}{Z'_n(s)+Z_{\text{m-sc}}(s)}\right]^{-1} \tag{17}$$

In the next step, the transformation to the frequency domain was performed by substituting $s = \text{j}2\pi f$. This enabled the generation of the analytical model frequency characteristics up to 1 MHz. Fig. 11 presents three characteristics: the simulation model, experimental measurements, and the analytical model. These characteristics were determined for the open-circuit condition from the S2 terminals. The proposed analytical model provides good fitting to the characteristics obtained from the simulation model and the experimental measurements within the analyzed frequency range.

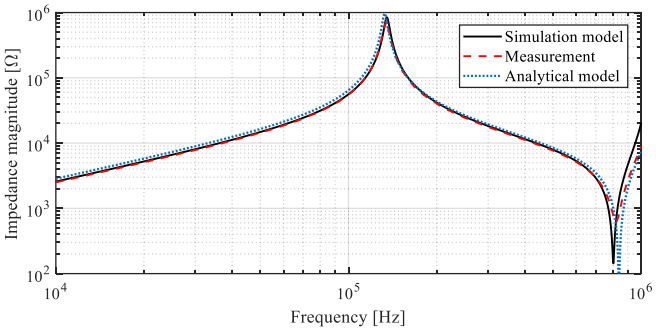


Fig. 11. Transformer impedance frequency characteristics under open-circuit conditions at the secondary-side winding (S*n*) up to 1 MHz, for the simulation model, the analytical model, and measurements performed on the fabricated transformer

V. Intrawinding Capacitance Reduction

The transformer employs a two-leg core structure. Custom ferrite cores made of 3C94 material (Ferroxcube) were used. The bobbins were manufactured using SLS additive manufacturing from polyamide, which is characterized by high dielectric strength [20]. Each secondary winding (S*n*) was sectioned to improve the insulation operating conditions associated with a more favorable electric field distribution between adjacent turns, layers, and winding sections. The transformer winding arrangement is presented in the longitudinal cross-section of the 1P2S structure shown in Fig. 12.

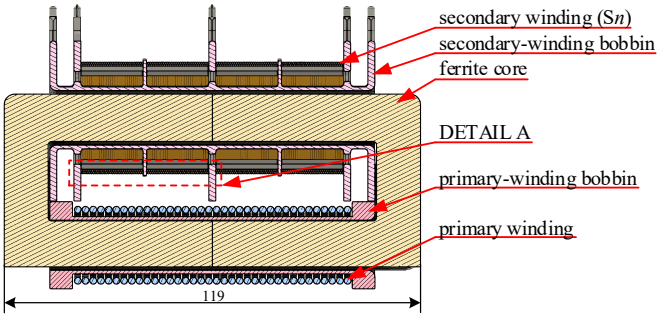


Fig. 12. Longitudinal cross-section of the transformer (single 1P2S structure), showing the bobbins and the primary and secondary windings

Fig. 13 presents the longitudinal cross-section of the secondary-side winding (S*n*) together with the bobbin. A significant spacing between the secondary winding and the core can be observed.

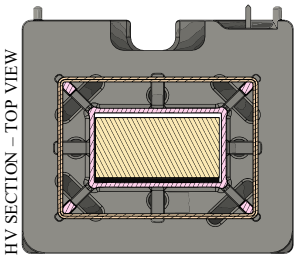


Fig. 13. Cross-sectional view of the transformer secondary side showing the winding arrangement with the windings offset from the core

During the simulation studies, the need to reduce the secondary-side (HV) transformer intrawinding capacitance was identified. This capacitance significantly affects the RMS current of the bridge transistors on the MV side. It causes additional energy circulation within the system, which directly impacts converter efficiency [21]. To mitigate this effect, a reverse-turn winding method was proposed, in which each subsequent winding layer starts again from the beginning of the section after completion of the previous layer. Fig. 14 presents the layered arrangement of the secondary-side winding implementing the reverse-turn winding method together with the indicated winding sequence.

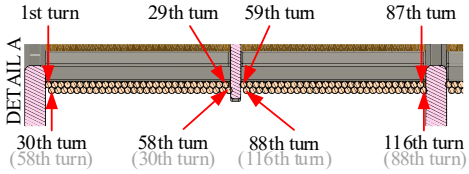


Fig. 14. Longitudinal cross-section of the transformer (DETAIL A) showing the layered, sectional arrangement of the secondary-side winding; the winding configuration characterized by higher secondary-side intrawinding capacitance is indicated by gray labels in parentheses

An alternative (simplified) winding arrangement is also indicated in Fig. 14 using gray labels in parentheses. Frequency-domain measurements were performed for two secondary-side winding arrangements. The measurements were carried out without the core and using only the secondary winding. The impedance frequency characteristics for both winding arrangements are presented in Fig. 15.

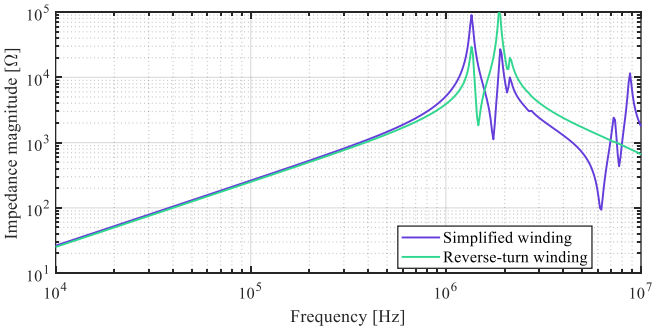


Fig. 15. Impedance frequency characteristics of the transformer secondary winding S*n* (without the core and primary winding) for the simplified and reverse-turn winding

The intrawinding capacitance measurements of the secondary-side winding confirmed the effectiveness of the reverse-turn winding approach. At 4 MHz, the measured capacitance decreased from 30.9 pF for the simplified winding arrangement to 16.7 pF for the reverse-turn winding, corresponding to a capacitance reduction of approximately 46%.

A similar sectioned high-voltage transformer structure was presented in [22]. In contrast to the transformer proposed in this work, the reported design employs a three-leg magnetic core assembled from U-shaped ferrite cores. A single primary winding is placed on the center leg, whereas two secondary winding sections are wound on each outer leg. Consequently, achieving the same voltage gain requires twice the number of secondary turns. The proposed 3×(1P2S) configuration enables a reduction in the number of secondary turns, which contributes to lower leakage inductance and reduced secondary-side intrawinding capacitance.

VI. Voltage Gain Characteristic

In addition to the transformer discussed previously, the overall resonant tank comprises a resonant capacitor and a common-mode choke (CMC). To determine the voltage-gain characteristics of the resonant converter, the parameters of both components were identified. Fig. 16 presents the impedance frequency characteristics of the resonant capacitor and the CMC responses for CM and DM excitations. For the analyzed converter, and particularly for the voltage-gain characteristics, the DM response of the CMC is of primary importance, as it is mainly associated with the leakage inductance of the choke. As reported in the literature, the DM response of a CMC is governed by its leakage inductance, whereas the CM response is associated with the magnetizing inductance [18].

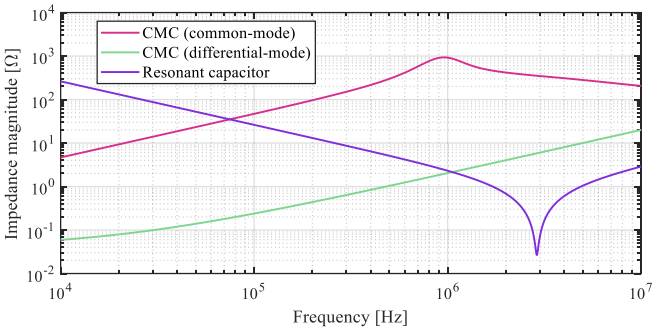


Fig. 16. Impedance frequency characteristics of the common-mode choke (CMC) for CM and DM responses, and of the resonant capacitor

The resonant capacitor has a capacitance of approximately 60 nF. In the experimental setup, it was implemented using six polypropylene capacitors intended for pulse applications, each rated at 10 nF and 1600 V DC. It should be noted that the capacitance C_s indicated in Fig. 5 and Fig. 6 corresponds to a single 1P2S structure. Therefore, for the analysis of a single structure, the value C_s = 20 nF should be assumed. Only for the complete 3×(1P2S) configuration should the total capacitance be considered as $3C_s$ (Fig. 4).

The determination of the resonant converter voltage-gain characteristics requires the definition of appropriate parameters describing the operation of the resonant tank. The normalized frequency f_n, defined by (18), is expressed as the ratio of the resonant tank operating frequency to the base frequency $f_0 = 151.5$ kHz. To simplify the notation of the equations, an equivalent inductance value $L_{\sigma ev}$ was introduced in (19). The value of f_0 was determined using (20). The quality factor Q was defined as the ratio of the characteristic impedance of the resonant circuit to the secondary-side load resistance R_{pnL} [23]. The expression used to determine the quality factor Q is given in (21). The expression describing the voltage gain M is presented in (22).

$$f_n = \frac{f}{f_0} \tag{18}$$

$$L_{\sigma ev} = L_{\sigma 0} + \frac{L'_{\sigma n}}{2} = L_{\sigma 0} + \frac{L_{\sigma n} z_p^2}{2 z_s^2} \tag{19}$$

$$f_0 = \frac{1}{2\pi\sqrt{L_{\sigma ev} C_s}} \tag{20}$$

$$Q = \frac{z_s^2 \sqrt{L_{\sigma ev} / C_s}}{z_p^2 R_{pnL}} \tag{21}$$

$$M = \frac{u'_1}{u_0} = \frac{u'_2}{u_0} = \frac{u'_n}{u_0} = \frac{z_p u_n}{z_s u_0} \tag{22}$$

The voltage-gain characteristics for different quality factor Q values as a function of the normalized frequency f_n are presented in Fig. 17. In the target system, the operating range corresponds to frequencies from 0.5 f_n to 0.85 f_n (75.8 to 128.8 kHz). As can be observed, the converter is capable of achieving high voltage-gain values for frequencies above approximately 2 f_n. However, it should be noted that in this operating region the amplitude of the primary-side winding current increases again, also for high load-resistance values, including no-load conditions (Fig. 18).

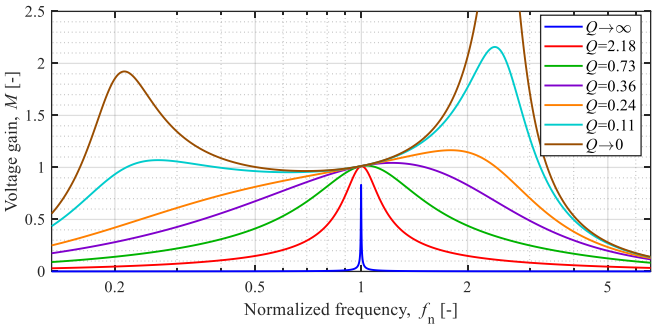


Fig. 17. Voltage gain characteristics of the HV resonant converter for different quality factor Q values as a function of normalized frequency f_n

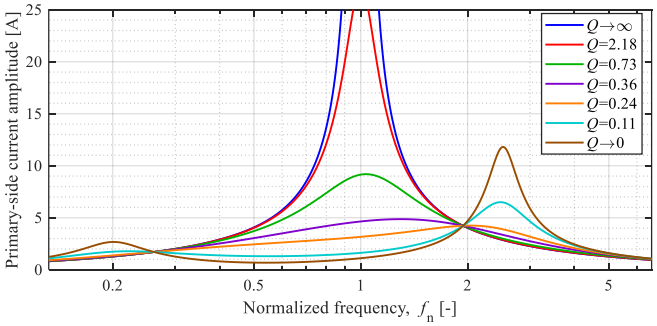


Fig. 18. Primary-side winding current amplitude characteristics of the HV converter for different values of the quality factor Q as a function of the normalized frequency f_n

The developed converter employs a hybrid control method combining switching-frequency modulation and duty-cycle control [24]. The adopted approach extends the achievable regulation range while simultaneously reducing the required switching-frequency span, which is particularly beneficial for high-voltage resonant converter operation.

In the context of the need to reduce the capacitance C_{pn}, it is also important to consider the influence of the rectifier diode junction capacitance C_j on the frequency characteristics and voltage-gain characteristics of the converter. The applied GC05MPS33J diodes exhibit a junction capacitance C_j of 14 pF for blocking voltages above 1700 V. In the analyzed bridge output stage (Fig. 2), the capacitance C_j is connected in parallel with C_{pn}. Therefore, to simplify the analysis of its impact on the converter functional characteristics, its effect was considered together with the influence of the intrawinding capacitance C_{pn}. The voltage-gain characteristics illustrating the influence of Cpn are presented in Fig. 18. It should be noted, however, that C_j is nonlinear and increases with decreasing reverse voltage, which significantly affects the converter characteristics [25].

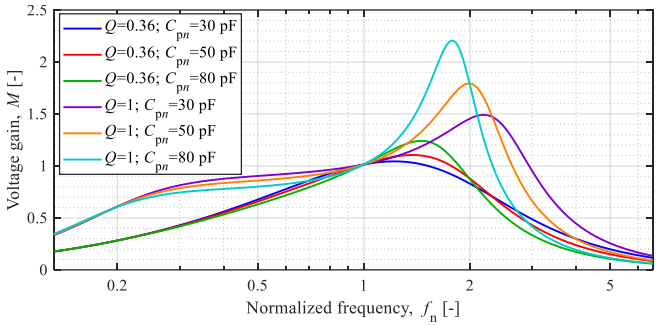


Fig. 19. Voltage gain characteristics of the HV resonant converter versus normalized frequency f_n for different values of the quality factor Q and secondary-side intrawinding capacitance C_{pn}

VII. Conclusion

The design of high-voltage DC–DC converters with a high voltage step-up ratio employing a transformer-based intermediate circuit constitutes a significant engineering challenge due to the need to ensure an adequate insulation system while maintaining the required converter operating performance. The design of transformers operating as part of a resonant circuit differs from typical commercial solutions, mainly due to the need to implement measures leading to increased leakage inductance, such as separation of the primary and secondary windings onto separate core legs, increased spacing between the windings and the core, and winding sectioning. The conducted investigations demonstrated a significant influence of the secondary-side intrawinding capacitance on the converter operating conditions. This capacitance causes additional energy circulation within the system, directly affecting converter efficiency. To mitigate this phenomenon, a reverse-turn winding arrangement was proposed. Furthermore, each secondary winding (Sn) was sectioned to improve the dielectric insulation conditions associated with a more favorable electric field distribution between adjacent turns, layers, and winding sections. The proposed extended equivalent circuit and the developed analytical model showed good agreement with experimental measurements.

References

[1] V. K. Sundaramoorthy, A. Mihaila, L. Spejo, R. Minamisawa, and L. Knoll, "Performance Comparison of 6.5 kV SiC PiN Diode with 6.5 kV SiC JBS and Si Diodes," Mater. Sci. Forum, vol. 1062, pp. 588–592, May 2022.

[2] R. Barlik and M. Nowak, Energoelektronika: elementy, podzespoły, układy. Warszawa: Oficyna Wydawnicza Politechniki Warszawskiej, 2014.

[3] Y. Li, M. ul-Hassan, A. B. Mirza, Y. Xie, S. Deng, S. S. Vala, F. Luo, X. Feng, S. V. J. Narumanchi, and J. D. Flicker, "State-of-the-Art Medium- and High-Voltage Silicon Carbide Power Modules, Challenges and Mitigation Techniques: A Review," IEEE Trans. Compon., Packag. Manuf. Technol., vol. 14, no. 12, pp. 2177–2195, 2024.

[4] X. Li, Y. Chen, H. Chen, R. Paul, X. Song, and H. A. Mantooth, "A 10 kV SiC MOSFET Power Module With Optimized System Interface and Electric Field Distribution," IEEE Trans. Power Electron., vol. 39, no. 8, pp. 9540–9553, 2024.

[5] I. Priyanti, D. Wongsawaeng, K. Ngaosuwan, W. Kiatkittipong, P. Hosemann, and S. Assabumrungrat, "Corona discharge plasma for green de-inking of inkjet printer ink," Sci. Rep., vol. 14, no. 1, p. 13035, 2024.

[6] J. Mucko, R. Dobosz, and R. Strzelecki, "Dielectric Barrier Discharge Systems with HV Generators and Discharge Chambers for Surface Treatment and Decontamination of Organic Products," Energies, vol. 13, no. 19, 2020.

[7] T. Sugihara, S. Nagai, and A. Kaneko, "High-aspect nano-groove fabrication in thick film resists using 150-kV high acceleration voltage electron beam lithography," Precis. Eng., vol. 74, pp. 205–208, 2022.

[8] Z. Satbayeva, B. Rakhadilov, Z. Turar, N. Berdimuratov, D. Baizhan, and A. Maulit, "Surface Modification of Chromium–Nickel Steel by Electrolytic Plasma Nitriding Method," Crystals, vol. 14, no. 9, 2024.

[9] [15] E. J. M. Van Heesch, T. Huiskamp, K. Yan, F. J. C. M. Beckers, H. W. M. Smulders, G. J. J. Winands, R. H. P. Lemmens, P. P. M. Blom, S. Davalos Segura, W. F. L. M. Hoeben, S. V. B. Van Paasen, J. J. Van Oorschot, A. G. A. Bonkestoter, M. L. J. Van Den Brand, M. Hennink, R. W. J. Smulders, A. J. M. Pemen, and P. C. T. Van Der Laan, "Pulsed processing by cold plasma, applied to industrial emission control," Front. Chem., vol. 12, 2024.

[10] H. Zhou, W. Peng, W. Huang, N. Ye, and C. Dong, "Performance of Miniature Carbon Nanotube Field Emission Pressure Sensor for X-Ray Source Applications," Micromachines, vol. 16, no. 7, 2025.

[11] W. Zhao, G. W. Lagerweij, B. Hurkmans, and M. G. Niasar, "Design of a High-Voltage Arbitrary Waveform Generator Using a Modular Cascaded H-Bridge Topology," Electronics, vol. 13, no. 22, 2024.

[12] S. Yin, Z. Zeng, S. Debnath, and M. Saeedifard, "Modeling and ZVS Operation of the Isolated Modular Multilevel DC–DC Converter With a Unified Trapezoidal Wave Modulation," IEEE Trans. Power Electron., vol. 39, no. 7, pp. 8306–8322, 2024.

[13] Z. Pei, D. Kong, C. Liu, C. Liu, D. Guo, D. Zhu, Y. Sun, and M. L. Heldwein, "Hybrid Isolated Modular Multilevel Converter Based Solid-State Transformer Topology With Simplified Power Conversion Process and Uneven Voltage Ratio," IEEE Trans. Power Electron., vol. 38, no. 10, pp. 12757–12773, 2023.

[14] S.-H. Min, H. Jung, O. Kwon, M. Sattorov, S. Kim, S.-H. Park, D. Hong, S. Kim, C. Park, B. H. Hong, I. Cho, S. Ma, M. Kim, Y. J. Yoo, S. Y. Park, and G.-S. Park, "Analysis of Electromagnetic Pulse Effects Under High-Power Microwave Sources," IEEE Access, vol. 9, pp. 136775–136791, 2021.

[15] W. Wang, X. Wang, J. He, Y. Liu, S. Li, and Y. Nie, "Electric stress and dielectric breakdown characteristics under high-frequency voltages with multi-harmonics in a solid-state transformer," Int. J. Electr. Power Energy Syst., vol. 129, p. 106861, 2021.

[16] T. Guillod, R. Faerber, D. Rothmund, F. Krismer, C. M. Franck, and J. W. Kolar, "Dielectric Losses in Dry-Type Insulation of Medium-Voltage Power Electronic Converters," IEEE J. Emerg. Sel. Top. Power Electron., vol. 8, no. 3, pp. 2716–2732, 2020.

[17] L. Liu, N. Ren, J. Wu, Z. Zhu, H. Xu, Q. Guo, and K. Sheng, "Investigation of Avalanche Capability of 1200 V 4H-SiC MPS Diodes

and JBS Diodes," in Proc. 32nd Int. Symp. Power Semicond. Devices ICs (ISPSD), 2020, pp. 210–213.

[18] P. González-Vizuete, C. Domínguez-Palacios, J. Bernal-Méndez, and M. A. Martín-Prats, "Simple Setup for Measuring the Response to Differential Mode Noise of Common Mode Chokes," Electronics, vol. 9, no. 3, 2020.

[19] L. Yu, S. Vudayagiri, L. Jensen, and A. Skov, "Temperature dependence of dielectric breakdown of silicone-based dielectric elastomers," International Journal of Smart and Nano Materials, vol. 11, pp. 1–18, 2020.

[20] D. M. French, J. P. O'Loughlin, B. W. Hoff, S. Maestas, D. Lepell, and T. Montoya, "Dielectric strength testing of 3D printed plastics and application to a high voltage transformer pulser," in 2015 IEEE Pulsed Power Conference (PPC), 2015, pp. 1–6.

[21] S.-S. Park, M.-S. Jeon, S.-S. Min, and R.-Y. Kim, "High-Frequency Planar Transformer Based on Interleaved Serpentine Winding Method With Low Parasitic Capacitance for High-Current Input LLC Resonant Converter," IEEE Access, vol. 11, pp. 84900–84911, 2023.

[22] J. Rąbkowski, A. Łasica, M. Zdanowski, G. Wrona, and J. Starzyński, "Portable DC Supply Based on SiC Power Devices for High-Voltage Marx Generator," *Electronics*, vol. 10, no. 3, 2021.

[23] Y. Shen, W. Zhao, Z. Chen, and C. Cai, "Full-Bridge LLC Resonant Converter With Series-Parallel Connected Transformers for Electric Vehicle On-Board Charger," IEEE Access, vol. 6, pp. 13490–13500, 2018.

[24] H. Jiang and X. Yue, "Phase-Shifting Adaptive LLC Resonant Converter with Reduced Turn-Off Loss in Wide Voltage Application," Energies, vol. 17, no. 7, 2024.

[25] S. Zhang, Z. Li, M. Xu, T. Luo, P. Sun, Q. Luo, J. Liu, and Y. Wei, "An Accurate Dynamic Time-Domain Model for LLC Resonant Converter by Considering Nonideal Components, Various Modulation Strategies, and Dynamic Process," IEEE J. Emerg. Sel. Top. Power Electron., vol. 13, no. 3, pp. 3119–3137, 2025.